

The K1.8BR spectrometer system at J-PARC

Keizo AGARI¹, Shuhei AJIMURA², George BEER³, Hyoungchan BHANG⁴, Mario BRAGADIREANU⁵, Paul BUEHLER⁶, Luigi BUSO^{7,8}, Michael CARGNELLI⁶, Seonho CHOI⁴, Catalina CURCEANU⁹, Shun ENOMOTO¹⁰, Diego FASO^{7,8}, Hiroyuki FUJIOKA¹¹, Yuya FUJIWARA¹², Tomokazu FUKUDA¹³, Carlo GUARALDO⁹, Tadashi HASHIMOTO¹², Ryugo S. HAYANO¹², Toshihiko HIRAIWA¹¹, Erina HIROSE¹, Masaharu IEIRI¹, Masami IIO¹, Mihai ILIESCU⁹, Kentaro INOUE¹⁰, Yosuke ISHIGURO¹¹, Takashi ISHIKAWA¹², Shigeru ISHIMOTO¹, Tomoichi ISHIWATARI⁶, Kenta ITAHASHI¹⁴, Masaaki IWAI¹, Masahiko IWASAKI^{15,14}, Yutaka KAKIGUCHI¹, Yohji KATOH¹, Shingo KAWASAKI¹⁰, Paul KIENLE¹⁶, Hiroshi KOU¹⁵, Johann MARTON⁶, Yasuyuki MATSUDA¹⁷, Michifumi MINAKAWA¹, Yutaka MIZOI¹³, Ombretta MORRA⁷, Ryotaro MUTO¹, Tomofumi NAGAE¹¹, Megumi NARUKI¹, Hiroyuki NOUMI², Hiroaki OHNISHI¹⁴, Shinji OKADA¹⁴, Haruhiko OUTA¹⁴, Kristian PISCICCHIA⁹, Marco POLI LENER⁹, Antonio ROMERO VIDAL⁹, Yuta SADA¹¹, Atsushi SAKAGUCHI¹⁰, Fuminori SAKUMA^{14*}, Masaharu SATO¹², Yoshinori SATO¹, Shin'ya SAWADA¹, Alessandro SCORDO⁹, Michiko SEKIMOTO¹, Hexi SHI¹², Yoshihisa SHIRAKABE¹, Diana SIRGHI^{9,5}, Florin SIRGHI^{9,5}, Ken SUZUKI⁶, Shoji SUZUKI¹, Takatoshi SUZUKI¹², Yoshihiro SUZUKI¹, Hitoshi TAKAHASHI¹, Kazuhiro TANAKA¹, Nobuaki TANAKA¹, Hideyuki TATSUNO⁹, Makoto TOKUDA¹⁵, Akihisa TOYODA¹, Dai TOMONO¹⁴, Akihisa TOYODA¹, Kyo TSUKADA¹⁸, Oton VAZQUEZ DOCE^{9,19}, Hiroaki WATANABE¹, Eberhard WIDMANN⁶, Barbara K. WÜNSCHEK⁶, Yutaka YAMANOI¹, Toshimitsu YAMAZAKI^{12,14}, Heejoong YIM²⁰, and Johann ZMESKAL⁶

¹*High Energy Accelerator Research Organization (KEK), Tsukuba, 305-0801, Japan*

²*Research Center for Nuclear Physics (RCNP), Osaka University, Osaka, 567-0047, Japan*

³*Department of Physics and Astronomy, University of Victoria, Victoria BC V8W 3P6, Canada*

⁴*Department of Physics, Seoul National University, Seoul, 151-742, South Korea*

⁵*National Institute of Physics and Nuclear Engineering - IFIN HH, Romania*

⁶*Stefan-Meyer-Institut für subatomare Physik, A-1090 Vienna, Austria*

⁷*INFN Sezione di Torino, Torino, Italy*

⁸*Dipartimento di Fisica Generale, Università di Torino, Torino, Italy*

⁹*Laboratori Nazionali di Frascati dell' INFN, I-00044 Frascati, Italy*

¹⁰*Department of Physics, Osaka University, Osaka, 560-0043, Japan*

¹¹*Department of Physics, Kyoto University, Kyoto, 606-8502, Japan*

¹²*Department of Physics, The University of Tokyo, Tokyo, 113-0033, Japan*

¹³*Laboratory of Physics, Osaka Electro-Communication University, Osaka, 572-8530, Japan*

¹⁴*RIKEN Nishina Center, RIKEN, Wako, 351-0198, Japan*

^{*}) E-mail: sakuma@ribf.riken.jp

¹⁵*Department of Physics, Tokyo Institute of Technology, Tokyo, 152-8551, Japan*

¹⁶*Technische Universität München, D-85748, Garching, Germany*

¹⁷*Graduate School of Arts and Sciences, The University of Tokyo, Tokyo, 153-8902, Japan*

¹⁸*Department of Physics, Tohoku University, Sendai, 980-8578, Japan*

¹⁹*Excellence Cluster Universe, Technische Universität München, D-85748, Garching, Germany*

²⁰*Korea Institute of Radiological and Medical Sciences (KIRAMS), Seoul, 139-706, South Korea*

A new spectrometer system was designed and constructed at the secondary beam-line K1.8BR in the hadron hall of J-PARC, in order to investigate $\bar{K}N$ interactions and \bar{K} -nuclear bound systems. The spectrometer consists of a high precision beam line spectrometer, a liquid helium target system, a Cylindrical Detector System that surrounds the target to detect the decay particles from the target region, and a neutron time-of-flight counter array located ~ 15 m away from the target position. Details of the design, construction, and performance of the detector components are described.

§1. Introduction

The physics goal of experiments at the secondary beam-line K1.8BR in the hadron hall of J-PARC is to investigate $\bar{K}N$ interactions and \bar{K} -nuclear bound states. The $\bar{K}N$ interaction has been figured out to be strongly attractive by extensive measurements of the anti-kaonic hydrogen atom¹⁾ and low-energy K^-N scattering.²⁾ However, the $\bar{K}N$ interaction and \bar{K} -nuclear bound states are still under debate. One of the biggest issues is on the location and structure of the $\Lambda(1405)$, whose traditional mass is located 27 MeV below the $\bar{K}N$ threshold. This resonance has been interpreted as an $I = 0$ quasi-bound state, embedded in the $\Sigma - \pi$ continuum. In recent years, strongly attractive $\bar{K}N$ interactions were deduced from a coupled-channel approach based on the ansatz that the K^-p bound state is located at 1405 MeV/ c^2 , and were used to predict strongly bound \bar{K} nuclear states.^{3),4)} On the other hand, theories based on chiral dynamics claim that the K^-p quasi-bound state should be located at 1420 MeV or higher, which results in a much shallower binding scheme, predicting much weaker bound \bar{K} systems.⁵⁾

At present, experimental data are not sufficient to discriminate among a variety of conflicting interpretations.^{6),7)} Therefore, new experimental data are eagerly awaited, and especially experiments using the elementary \bar{K} induced reaction are expected to clarify the puzzling $\bar{K}N$ interactions. At the K1.8BR beamline of J-PARC, three new experiments with the K^- beam were proposed and approved:

E15

The E15 experiment searches for the simplest kaonic nuclear bound state, K^-pp , which was predicted³⁾ by the in-flight ${}^3\text{He}(K^-, n)$ reaction.⁸⁾ The experiment provides crucial data for kaonic nuclei by performing exclusive measurements: a missing-mass spectroscopy using the emitted neutron, and invariant-mass spectroscopy via the expected decay $K^-pp \rightarrow \Lambda p \rightarrow p\pi^-p$.

If both binding energy and width of the K^-pp bound state are assumed to be

around $100 \text{ MeV}/c^2$ as indicated by recent experimental results,⁷⁾ the missing mass resolution of the (K^-, n) reaction is required to be less than $10 \text{ MeV}/c^2$ (σ) in order to discriminate the K^-pp signal from physical backgrounds such as the two nucleon absorption processes from the $K^-+{}^3\text{He}$ interactions. For the invariant-mass spectroscopy, a large acceptance detector surrounding the target system is essential. Requirement for the detector is to identify secondary charged particles from the target and to reconstruct the $K^-pp \rightarrow \Lambda + p$ decay with invariant-mass resolution of less than $20 \text{ MeV}/c^2$ (σ), in order to separate the expected K^-pp decay modes of $\Lambda + p$ and $\Sigma^0 + p$. Additional information on the other decay channels such as $p + \Sigma + \pi$ will also be studied.

E17

The E17 experiment clarifies the isospin dependence of the K^- -nucleus strong interaction at the low energy limit.⁹⁾ By using high-resolution silicon drift X-ray detectors (SDDs), the experiment is able to measure the strong-interaction induced shift of $3d \rightarrow 2p$ X-rays from $K^-{}^3\text{He}$ and $K^-{}^4\text{He}$ atoms with the world's highest precision.

In order to carry out the high precision measurement of the X rays, the SDDs are required to have energy resolution of better than $\sim 185 \text{ eV}$ (FWHM) at 6.4 keV which was achieved in the previous experiment KEK-PS E570.¹⁰⁾ In addition, for background reduction, the reaction vertex should be reconstructed by using the beam line detectors and the tracking detectors surrounding the target.

E31

The primary goal of the E31 experiment is exclusively to show the spectral function of the $\Lambda(1405)$ resonance produced in the $\bar{K}N \rightarrow \pi\Sigma$ channel via the in-flight (K^-, n) reaction on the deuteron.¹¹⁾

The experimental requirements of E15 also satisfy those of E31. In addition to the E15 request, E31 requires the detection and identification of a backward going proton from the $\Lambda(1405) \rightarrow \Sigma^0 + \pi^0$ decay in order to measure all the $\Sigma^+\pi^-$, $\Sigma^-\pi^+$, and $\Sigma^0\pi^0$ final states from the $\Lambda(1405)$ decay.

A dedicated spectrometer was designed and constructed at the K1.8BR beam line to satisfy all the above experimental requirements. The spectrometer consists of a high precision beam line spectrometer, a liquid helium target system, a Cylindrical Detector System (CDS) that surrounds the target to detect the decay particles from the target region, and a neutron time-of-flight counter array located $\sim 15 \text{ m}$ away from the target position, as shown in Fig. 1.

In the following, a brief overview of the detector system at K1.8BR is provided, and then details of the design, construction, and performance of experimental components are described.

§2. Detector overview

The secondary beam line K1.8BR was constructed at the hadron hall of the J-PARC 50 GeV Proton Synchrotron (PS). The 30 GeV primary proton beam accel-

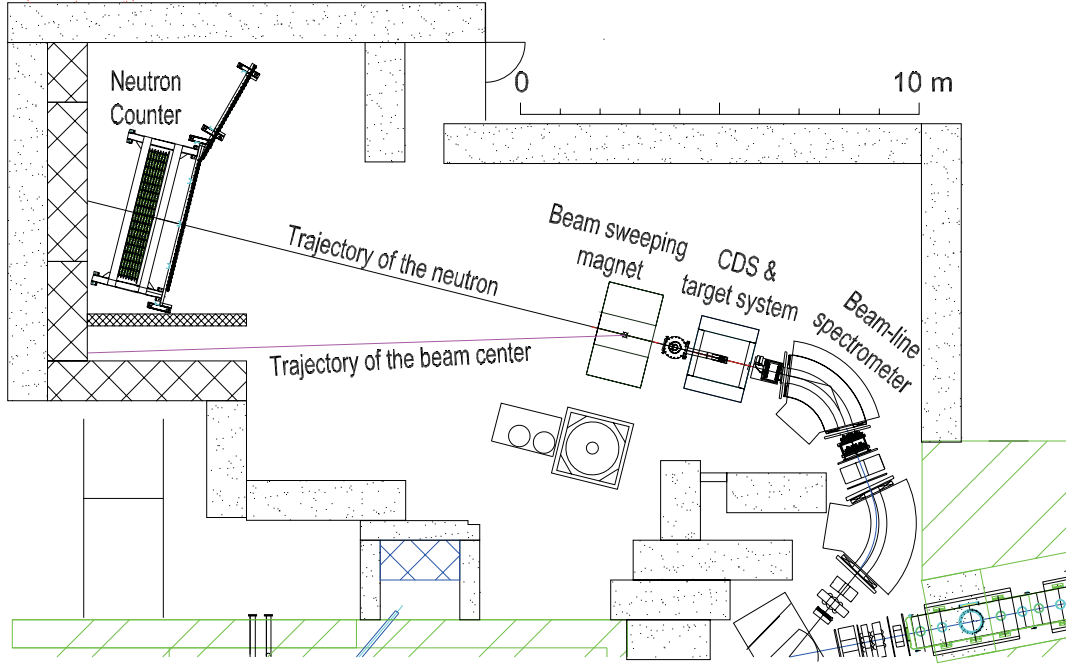


Fig. 1. Schematic view of the K1.8BR spectrometer. The spectrometer consists of the beam line spectrometer, the Cylindrical Detector System that surrounds the liquid ^3He target system to detect the decay particles from the target region, the beam sweeping magnet, and the neutron time-of-flight counter located ~ 15 m away from the target position.

erated by the PS is transported to the hadron hall through the beam switching yard and focused on the secondary-particle-production target T1. The K1.8BR beam line is branched from K1.8 at a bending magnet downstream of an electrostatic separator ESS1 which purifies the secondary particles. The K1.8BR beam line is designed to deliver separated charged particles with momentum up to $1.2 \text{ GeV}/c$. The configuration of the K1.8BR beam line is shown in Fig. 2 and its parameters are summarized in Table I. The length of the K1.8BR beam line is 31.5 m, which has great advantage for low-momentum kaon transportation. The intensity of the $1.0 \text{ GeV}/c$ K^- beam is expected to be 2×10^6 per spill (6 seconds repetition) based on an estimation using the Sanford-Wang formula¹²⁾ where the operation beam power for the PS and the production target are assumed to be 270 kW and 54mm thickness nickel target, respectively.

The beam-line spectrometer is composed of beam line magnets, trigger counters, beam trackers, and a kaon identification counter. The beam line magnets are comprised of an SQDQD system, and are located downstream of a branching magnet D3. The beam trigger is generated by two trigger counters located downstream of the D3 and the D5 magnet, respectively, whose flight length is 7.7 m. The kaon beam of momentum around $1.0 \text{ GeV}/c$ is identified by using a kaon identification counter. Trajectory of the kaon beam is tracked with the two beam line chambers installed across the D5 magnet. The momentum of the kaon is analyzed using this tracking

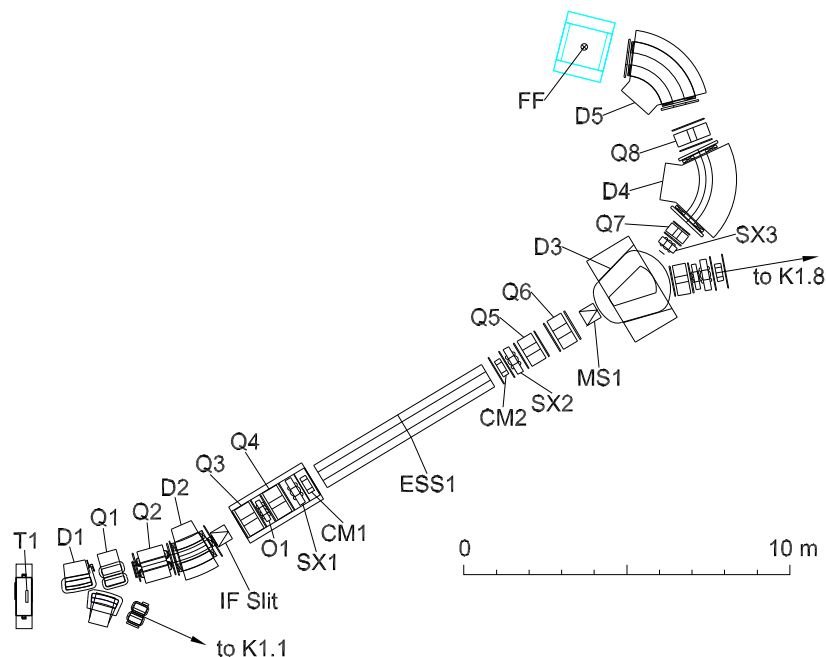


Fig. 2. Configuration of the K1.8BR beam line in the hadron hall of J-PARC.

Table I. Parameters of the K1.8BR beam line.

Primary beam	30 GeV/c proton
Repetition cycle	6 sec
Flat Top	2.93 sec
Production target	Pt(50% loss) / Ni(30% loss)
Production angle	6 degrees
Length (T1-FF)	31.5 m
Momentum range	1.2 GeV/c max.
Acceptance	2.0 msr·% ($\Delta\Omega \cdot \Delta p/p$)
Momentum bite	± 3 %

information together with beam optics of the D5 beam line magnet. The expected momentum resolution of the incident kaons with the beam-line spectrometer is ~ 0.1 %. The beam-line spectrometer was completed in January 2009, when the first beam was delivered to the J-PARC hadron hall.

The K^- beam is transferred to the liquid ^3He target system located at the final focus point; the CDS surrounds the target to detect the decay particles from the target. The target system has been developed for the E15 and E17 experiments, whose design is based on the techniques developed for the ^4He target used by KEK-PS E471, E549, and E570. In the stopped- K^- experiment E17, X-ray measurement is performed using the SDDs installed in the target chamber. A liquid D_2 target system has been developed also using almost the same design as the ^3He system, for the E31 experiment. The liquid ^3He target system was completed in 2008, and the SDDs were ready in 2010.

The decay particles from the target are detected by the CDS which has a solid angle coverage of 59% of 4π . Detailed tracking information of charged particles is obtained by a Cylindrical Drift Chamber (CDC) which operates in a magnetic field of 0.7 T provided by a solenoid magnet. Particle identification is given by a Cylindrical Detector Hodoscope (CDH) using time-of-flight (TOF) together with the trigger counter. The basic system of the CDS was completed in 2008, and new detectors for the CDS upgrade are under development now.

A forward neutron generated by the (in-flight K^-, n) reaction is detected by a forward neutron TOF counter array. TOF distance is optimized to be ~ 15 m from the target which will enable us to achieve a total missing mass resolution of $10 \text{ MeV}/c^2$ (σ) with ~ 150 ps TOF resolution of the system. To guarantee sufficient neutron detection efficiency, the incident beam which passes through the target is bent by a sweeping magnet placed just after the CDS. The neutron TOF counter and the sweeping magnet were installed in 2012.

§3. Beam-line detectors

A schematic view of the beam-line spectrometer is presented in Fig. 3. The beam-line spectrometer is composed of beam line magnets, trigger counters, beam trackers, and a kaon identification counter. The beam trigger is generated by the coincidence signal of a Beam Hodoscope Detector (BHD) and a Time Zero counter (T0), whose flight length between the BHD and T0 is 7.7 m. The kaon beam of momentum around $1.0 \text{ GeV}/c$ is identified by using an aerogel Cherenkov counter (AC) whose refractive index of the Cherenkov radiator is 1.05. Trajectory of the kaon beam is tracked with the two beam trackers, a PDC and a BLC, and the momentum of the kaon is analyzed with this tracking information together with beam optics of the D5 beam line magnet.

For E17, the stopped- K^- experiment, the kaon beam is degraded by carbon and copper blocks placed after T0. The degraded kaon is transferred into the liquid ^3He target through an energy measurement counter (E0) and a vertex beam-line drift chamber (VBDC), and stopped inside the target. The reaction vertex is obtained from an incident kaon and an outgoing secondary charged particle track reconstructed by the VBDC and the CDC, respectively. By applying a correlation cut between the reaction vertex in the beam direction and the energy loss in E0, in-flight kaon decay/reaction events are rejected and continuum background events are drastically reduced as a result.

3.1. Trigger counters

The BHD and T0 are segmented plastic scintillation counters located downstream of the D3 and the D5 magnet, respectively. The T0 signal is used as the event time-zero signal.

The BHD has an effective area of 400 mm (horizontal) \times 160 mm (vertical) segmented into 20 units horizontally, and T0 is 160 mm (horizontal) \times 160 mm (vertical) segmented into 5 units horizontally. To avoid over concentration of the beam on one segment, T0 is rotated by 45 degrees. The BHD scintillator is made

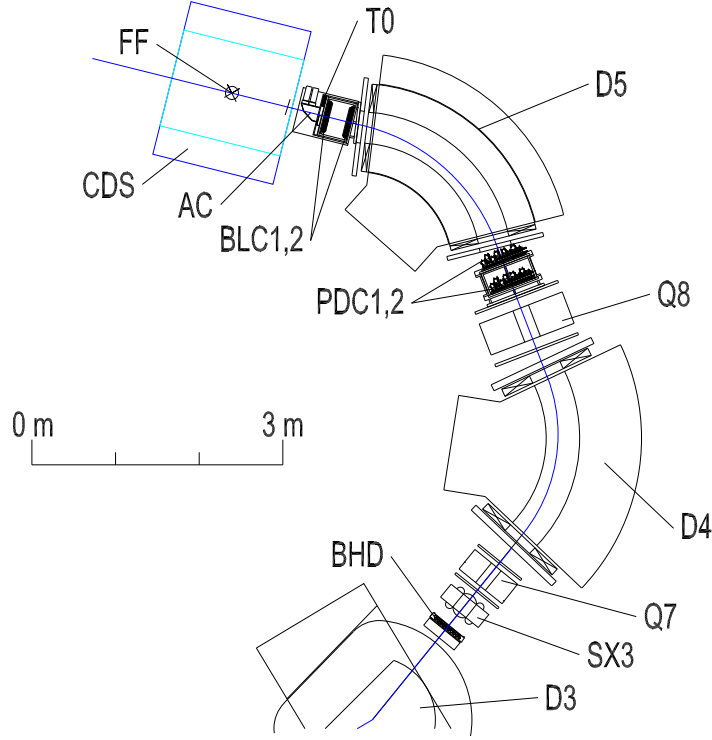


Fig. 3. Schematic view of the beam-line spectrometer, which consists of the trigger counters, the beam line chambers, and the kaon identification counter.

of Saint-Gobain BC412 whose unit size is 160 mm (height) \times 20 mm (width) \times 5 mm (thickness). The unit size of the Saint-Gobain BC420 scintillator in T0 is 160 mm (height) \times 32 mm (width) \times 10 mm (thickness). In both of the trigger counters, the scintillation light is transferred through light guides to a pair of 3/4 inch photomultipliers of H6612B made by Hamamatsu Photonics which are attached to the top and bottom ends through light guides. Since the coincidence rate of the top and bottom photomultipliers will reach ~ 1 M counts per spill, high voltage bleeders of all photomultipliers are modified to supply enough current to the last three dynodes.

Discriminated signals from the top and bottom photomultipliers are coincided and provide the timing of each segment. The TOF resolution between the BHD and T0 is observed to be typically 160 ps (σ) after a pulse-height correction is applied.

3.2. Kaon identification counter

In order to trigger the kaon beam, the AC located downstream of T0 is used to identify the kaon. Kaons in the momentum region from 0.9 GeV/ c to 1.1 GeV/ c , used for the experiments at K1.8BR, are clearly separated from pions.

The AC uses silica aerogel produced by Matsushita Electric Works Corp as SP-50 whose refractive index is 1.05. The AC has an effective area of 166 mm (width) \times 166 mm (height) \times 50 mm (thickness). Cherenkov photons radiated in the beam direction are reflected by forward optical mirrors and read out by four

photomultipliers as shown in Fig. 4. The photomultipliers are single-photoelectron sensitive H6559UVB of Hamamatsu Photonics with a photocathode diameter of 3 inches, whose window is made of UV-transparent glass. For 1.0 GeV/ c beam, the pion detection efficiency is 96 % at a threshold level of ~ 5 photoelectrons whereas the miss identification ratio of the kaon as the pion is 5.5 %.

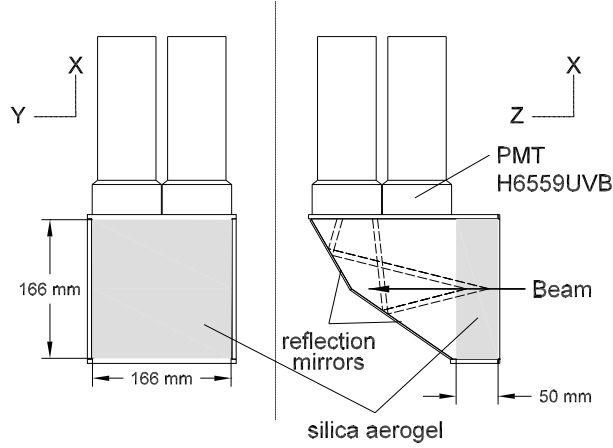


Fig. 4. Schematic view of the aerogel Cherenkov counter. Typical beam trajectories and Cherenkov light paths are shown.

3.3. Beam-line chambers

Tracking of the kaon beam is performed with the PDC and the BLC; these tracking chambers are installed across the D5 magnet. Both the PDC and the BLC are the same type of planar drift chamber.

The PDC consists of two sets of the same drift chamber, PDC1 and PDC2, which have 8 layers with a $UU'VV'UU'VV'$ configuration. In the U and V layers the wires are tilted by ± 45 degrees. Each layer contains 32 sense wires with a drift length of 4 mm corresponding to an effective area of $256 \text{ mm} \times 256 \text{ mm}$. The number of readout channels is 256 for both PDC1 and PDC2, which are installed 300 mm apart upstream of the D5 magnet.

The BLC is similar to the PDC; the BLC consists of two sets of the same drift chamber, BLC1 and BLC2. Each chamber has a $UU'VV'UU'VV'$ configuration and 32 sense wires per layer, i.e, the number of readout channels is 256 for both BLC1 and BLC2. In the U and V layers the wires are tilted by ± 45 degrees. A drift length is 2.5 mm corresponding to an effective area of $160 \text{ mm} \times 160 \text{ mm}$. BLC1 and BLC2 are installed 275 mm apart downstream of the D5 magnet.

Both the PDC and the BLC use a gold-plated Tungsten wire with 3 % Rhenium with a diameter of $12.5 \mu\text{m}$ and a Copper-Beryllium wire with a diameter of $75 \mu\text{m}$ for the sense and potential wires, respectively. To suppress multiple scattering of the beam kaons, the cathode planes are made of $1.5 \mu\text{m}$ aluminized Mylar. The read-out electronics of both chambers consist of a preamplifier card with Amplifier-Shaper-

Discriminator ICs (ASD, SONY-CXA3653Q,¹³⁾ $\tau = 16$ ns) mounted on the chambers, a LVDS-ECL converter, and a time to digital converter (TDC). The output signal of the ASD board is sent to the LVDS-ECL converter board via 7 m-long twisted-pair cables. From the LVDS-ECL converter, the signal is transferred to the counting house with 50 m-long twisted-pair cables. As a chamber gas, an argon-isobutane mixture is used through a methylal (dimethoxy-methane) bubbler at refrigerator temperature with the ratio of 76 % (Ar), 20 % (Isobutane) and 4 % (Methylal). The operation voltages of the PDC and the BLC are set to be -1.25 kV on the potential wires and the cathode planes. Typical position resolutions of 200 μm for both the PDC and the BLC have been obtained.

3.4. Detectors for the stopped- K^- experiment

E0, a segmented plastic scintillation counter which has an effective area of 102 mm (horizontal) \times 90 mm (vertical) segmented into 3 units horizontally, is located just downstream of the degraders. The E0 scintillator is made of Eljen EJ230 whose unit size is 102 mm (height) \times 30 mm (width) \times 20 mm (thickness). The scintillation light is transferred through light guides to a pair of 1 inch fine-mesh photomultipliers of H6152-01B made by Hamamatsu Photonics which are attached to the top and bottom ends. The high voltage bleeders of the photomultipliers are modified to supply enough current to the last three dynodes.

The VBDC is a planar drift chamber located just before the target system, hence was designed to be installable within the 30 cm inner diameter of the CDC. It is 250 mm in diameter and 73.2 mm in height and consists of 8 layers with a $UU'VV'UU'VV'$ configuration, where each layer contains 16 sense wires with a drift length of 2.5 mm corresponding to an effective area of 80 mm \times 80 mm. In the U and V layers the wires are tilted by ± 45 degrees. The sense and potential wires are the same as those for the beam line chambers. The cathode planes are made of 7.5 μm -thick Kapton, of which both sides are coated by 0.1 μm aluminum with a layer of 0.0025 μm chromium as protection against oxidization. The read-out electronics and gas mixture are as those for the beam line chambers.

For the in-flight experiments, E0 and the VBDC are replaced by the detectors for the CDS upgrade, the TGEM-TPC, the BPC, and the BPD, which are described later.

§4. Cryogenic target systems

In the experiments at the K1.8BR, a liquid ^3He and a liquid D_2 target are used in the J-PARC E15/E17 and E31 experiments, respectively. Both target systems are combined with the CDS, which is described later. To have large acceptance for the secondary charged particles, an L-shaped cryostat is adopted to place the target cell at the center of the CDS. In this section, we present an overview of both cryogenic target systems.

4.1. Liquid ^3He target system

4.1.1. Configuration and operational procedure

A schematic drawing of the liquid ^3He cryostat is illustrated in Fig. 5 for the case of the J-PARC E15 setup. The details of the ^3He target system can be found in a separate paper.¹⁴⁾ The major difference between the E15 and E17 settings is the configuration around the target cell. To maximize the acceptance for the kaonic helium X-rays in E17, eight silicon drift detectors (SDDs) are installed around the target cell as shown in the inset of Fig. 5. In contrast, a time projection chamber will be installed between the target vacuum chamber and the CDS in the E15 setup. Thus, the diameter of the vacuum chamber is minimized as much as possible. The major cryogenic component is divided into three sections; a ^4He separator, a ^4He evaporator and a heat exchanger between ^3He and ^4He . The target cell is connected to the bottom of the heat exchanger with two 1 meter long pipes. To reduce the radiation from room temperature components, all low-temperature parts are covered with a radiation shield anchored to the liquid nitrogen tank (LN_2 tank).

The operational concept of the cryostat of E15 and E17 is essentially the same. Typical start-up procedure begins with liquid nitrogen cooling. When the ^4He separator and the LN_2 tank are filled, the evaporator, the heat exchanger and the target cell are cooled by thermal conduction and radiation. After the pre-cooling, the liquid nitrogen in the separator is purged, and the liquid helium is transferred from a 1000 ℓ Dewar (not shown in the figure) to the separator by a transfer tube. The liquid flow is controlled by the pressure inside the separator evacuated by a dry pump. Liquid ^4He inside the separator is fed to the ^4He evaporator through a needle valve. The vapor pressure in the evaporator is reduced by a rotary pump with pumping speed of 120 m^3/h , resulting in a heat-removal capability of 2.5 W at 2 K. The temperature inside the evaporator is controlled within a range of 1.3 to 2.0 K. This range is mainly determined by the flow rate from the separator to the evaporator. The lowest temperature is achieved with no flow from the separator because the liquid temperature in the separator is fairly high (4.2 K). For liquefaction of ^3He , the heat exchanger between liquid ^4He and gaseous ^3He is positioned below the evaporator. The top part of the heat exchanger, where the liquid ^4He in the evaporator is in direct contact, has a specially-designed fin structure with both a width and pitch of 0.5 mm.

A gas-tight handling system (leak rate less than 10^{-10} Pa $\cdot\text{m}^3/\text{sec}$) has been constructed to store, transfer and recover the scarce ^3He gas. The total amount of 400 ℓ of gaseous ^3He is stored at pressures of less than an atmosphere at room temperature in two 200 ℓ tanks. During the cooling stage, those gas tanks are connected to the heat exchanger by the gas handling system. By an effective heat contact inside the heat exchanger, gaseous ^3He is liquefied, and the liquid ^3He is flowed to the target cell through the lower pipe. At the last stage of the cooling, most of the ^3He gas is liquefied inside the target cell and the heat exchanger.

In the L-shaped cryostat, the heat load on the target cell must be transferred effectively to the heat exchanger where the cooling power exists. Otherwise a boiling in the target cell occurs. To accomplish this, we applied the *siphon method* as

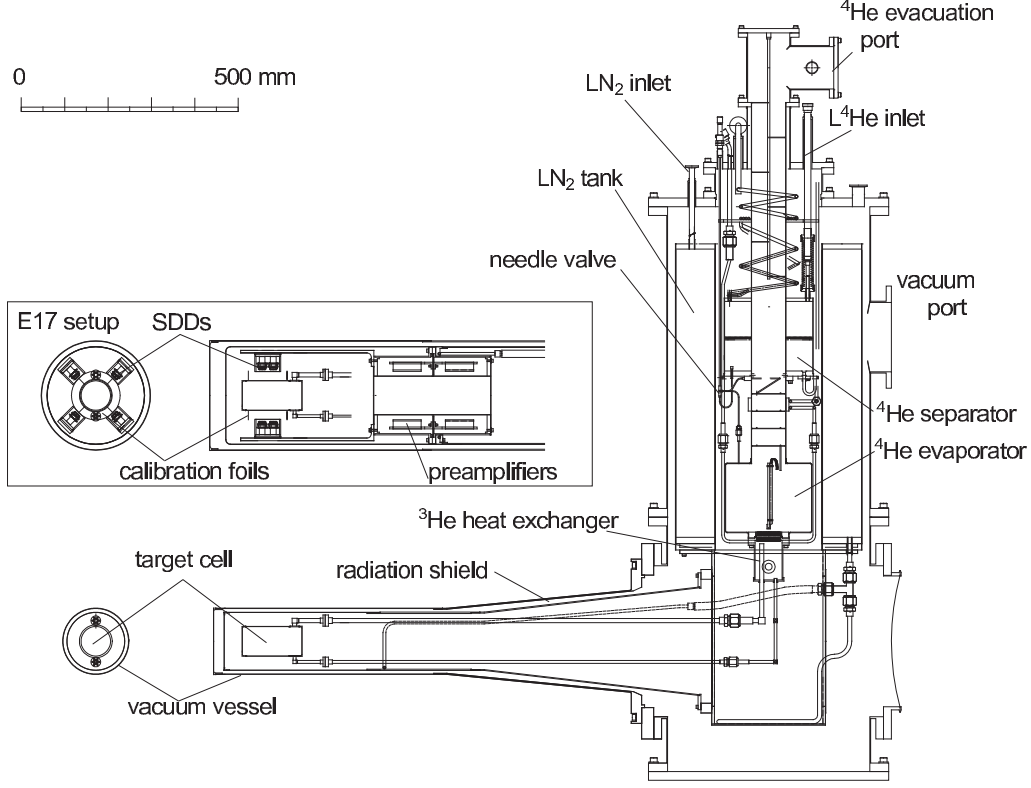


Fig. 5. Schematic drawing of the liquid ^3He cryostat.

described in Ref.^[14] which uses convection of the liquid ^3He . The liquid ^3He warmed by the heat load inside the target cell returns to the heat exchanger through an upper pipe. In the heat exchanger, ^3He is cooled again and fed to the target cell through the lower pipe. This makes possible the heat transfer between the target cell and the heat exchanger.

For long-term operation, it is essential to reduce the total amount of ^4He consumption. This is because exchanging the ^4He Dewar causes significant experimental dead time. To minimize the ^4He consumption, we adopted *one-shot* operation. This operation consists of two modes; (I) the evaporator is filled up with liquid ^4He supplied from the separator. (II) The ^4He supply is stopped until the evaporator becomes empty. The operational procedure consists of a repetition of these two methods, and this reduces the total liquid ^4He consumption due to the minimization of the transfer loss to the cryostat. The operational performance of the target system is described in the following.

4.1.2. Operation and performance

Along with the operational procedure previously described, cooling tests were performed. After the ^4He transfer, it took about 2 - 3 hours to liquefy the ^3He gas in the heat exchanger, achieving thermal equilibrium within 6 hours and a temperature of 1.3 K in the target cell without flow from the separator (mode (II) in the *one-shot* operation). The temperature differences among the evaporator, the heat exchanger and the target cell are less than 0.01 K. This means the heat transfer by *siphon method* is working well. Furthermore, the pressure inside the heat exchanger was identical to the vapor pressure of liquid ^3He at the corresponding temperature. Taking into consideration the remaining pressure inside the tanks, a total amount of 380 ℓ was condensed, giving evidence that sufficient ^3He gas is liquefied to fill the target.

From the reduction rate of the liquid ^4He in the evaporator, the heat load of the low-temperature region was estimated to be 0.21 W with the E15 setting. In the E17 setting, the heat load was expected to increase due to the radiation from the SDDs to the target. It was measured to be 0.39 W with the actual E17 setting, and both of them are acceptably small for long-term operation. The operational result of the cryostat with the E15 setting is tabulated below.

Table II. Operational result.

vacuum level	[mbar]	$< 10^{-6}$
leak rate of the ^3He system	[Pa·m ³ /sec]	$< 10^{-10}$
temperature in the target cell	[K]	1.3
vapor pressure in the target	[mbar]	33
heat load to low-temperature part	[W]	0.21
liquid ^4He consumption	(ℓ /day)	50

Finally, we note that this cryostat can be utilized as a liquid ^4He target system by liquefying gaseous ^4He instead of ^3He . The operational procedure and the performance of the liquid ^4He target are the same as those of ^3He .

4.2. Liquid D_2 target system

For a spectroscopic study of $\Lambda(1405)$ by the $d(K^-, n)$ reaction (J-PARC E31), we have been developing a liquid D_2 target system. A side-view of the cryostat is shown in Fig. 6. Since we measure the decay products of $\Lambda(1405)$, the target cell is isolated at the center of the CDS in the same way as the liquid ^3He cryostat. The major difference from the liquid ^3He target is that this cryostat is coolant-free. The key component of the system is a two-stage Gifford-McMahon (G-M) refrigerator (Sumitomo Heavy Industries, Ltd. RDK-145D and CSA-71A) built in the cryostat. The cooling power at the first and second stages is 35 W at 50 K and 1.5 W at 4.2 K, respectively. As it is for the ^3He target, a gas handling system has been constructed for the D_2 target. The 1000 ℓ of gaseous D_2 is stored in a tank at 2 bar at room temperature. To avoid contamination, the amount of D_2 gas was chosen to maintain positive pressure inside the gas system even after liquefaction in the target.

The D_2 gas is fed into the cryostat through the top flange. For pre-cooling, the

inlet pipe for the D_2 gas is anchored to a copper plate attached to the first-stage cold head of the G-M refrigerator. Another inlet pipe is directly connected through the top flange to the heat exchanger. It is used to measure the D_2 pressure inside the heat exchanger. Since this pipe has a larger conductance, a safety valve which prevents a sudden pressure rise is also connected to it. The D_2 gas is cooled in the heat exchanger where the second stage of the G-M refrigerator is thermally contacted. The structure of the heat exchanger is similar to that of the ^3He system.¹⁴⁾ The main difficulty in the operation of the system is the precise control of the temperature in the heat exchanger. In the liquid D_2 target system, the *siphon method*, described previously, is also adopted. For effective heat transfer between the target cell and the heat exchanger, D_2 must be kept in a liquid state by controlling the temperature to avoid blocking of pipes by solid D_2 . The temperature range of liquid D_2 is 18.7-23.8 K at 1 bar. The temperature should be kept around 20 K within acceptable limits. Since the cooling power of the second stage of the G-M refrigerator is larger than the heat load on the low-temperature parts, we have installed a heater near the cold finger to compensate the heat load. The current in the heater is controlled by a proportional-integral-derivative (PID) algorithm with an input of the temperature of the heat exchanger.

Until now, we have installed the G-M refrigerator and heat exchanger in the vertical part of the cryostat. Using hydrogen gas for convenience, preliminary tests were performed to confirm the temperature stability. In these tests, the target cell was directly connected to the heat exchanger. The result shows that the temperature of the heat exchanger is controlled within 0.2 K, which is sufficiently stable for the operation. By the summer in 2012, cooling tests will be performed on the final setup with the D_2 gas.

§5. Silicon drift X-ray detector

The goal of the E17 experiment is to achieve a precision measurement of both kaonic- ^3He and ^4He atoms with an unprecedented accuracy of 1 eV. To accomplish this precision, we employ Silicon Drift Detectors (SDDs) with a large active area. The concept of an SDD was originally introduced by E. Gatti and P. Rehak in 1984.¹⁶⁾ The electric field parallel to the surface of the detector is generated by ring electrodes biased gradually. Electrons created by incoming X-ray absorption are drifted toward a collection anode placed at the center of the detector. The distinguishing feature of SDDs is the extremely small anode size which results in low capacitance of the detector. It is also independent of the detector active area, thus large size of the active area of 100 mm² becomes possible with low capacitance. To take advantage of the low output capacitance, an FET for the first-stage amplification is directly integrated on the detector chip. It is connected to the anode with a short metal strip to minimize the stray capacitance and microphonic noise. A typical energy resolution of 150 eV is obtained at 6 keV with sufficient noise-reduction. The time resolution is typically sub-micro second below 200 K, which is mainly determined by the drift-time distribution of electrons in silicon. In recent years, several types of SDDs with a large active area have been developed. For X-ray spectroscopy of

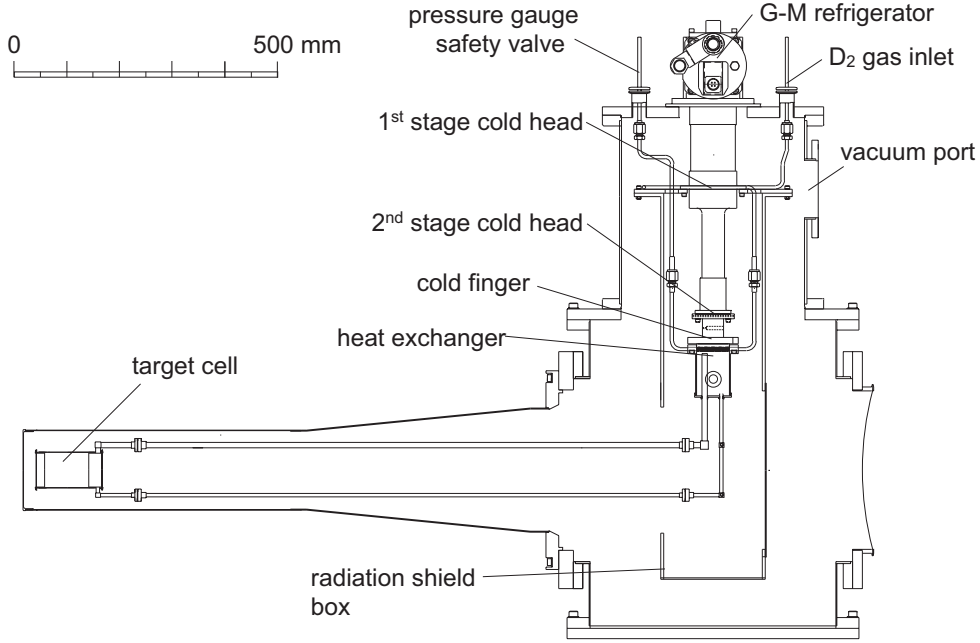


Fig. 6. Schematic drawing of the liquid D₂ cryostat.

kaonic atoms, SDDs were used in the KEK-PS E570 experiment in KEK,⁷ and the SIDDHARTA experiment in LNF.¹⁷⁾

In the J-PARC E17 experiment, 8 SDDs and reset-type preamplifiers developed by KETEK^{*)} were adopted. Each detector has a thickness of 0.45 mm and an active area of 100 mm². They are mounted around the liquid helium target as illustrated in the inset of Fig. 5. The acceptance for both kaonic ³He and ⁴He L_α X-rays is approximately 1 % with 8 SDDs taking into account the attenuation inside the helium target, the target cell and so on. The preamplifiers are also installed in vacuum to minimize the cable length between SDDs and preamplifiers. Output signal from the preamplifiers are connected to a CAEN N568b shaping amplifier. Semi-Gaussian outputs are provided with different shaping times of 0.5 and 3.0 μ s. Output signals with 0.5 μ s shaping time are used for the timing information of the SDDs in coincidence with an incoming K^- . Signals with 3.0 μ s shaping time are recorded with two types of peak-hold ADCs, TKO peak-hold ADC and VME CAEN V785. For the purpose of the pileup rejection, the line-shapes of the signals are also recorded by a flash ADC (SIS3301, 14 bit, 105MHz).

To reduce the heat loads on the helium target, SDDs must be operated at low temperature. We performed basic studies on the temperature dependence of the energy- and time- resolutions, and optimized the operational temperature of SDDs

*) KETEK GmbH, Vitus-SDD without window and collimator

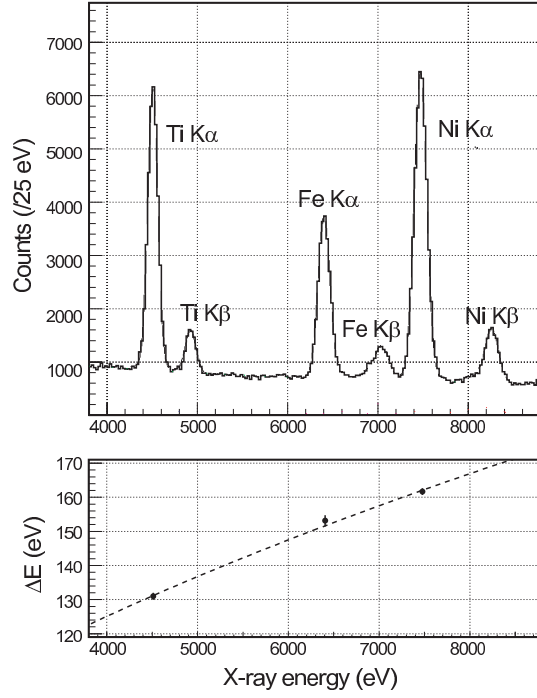


Fig. 7. A spectrum with fluorescence x-rays induced by beam at K1.8BR (Top) and the energy dependence of the energy resolution (Bottom). Dotted line represents an empirical formula described in the text.

to 130 K. All 8 SDDs were operated successfully inside the cryostat during cooling of the liquid ^4He target.

In November 2010, we performed commissioning of SDDs with the secondary beam at the K1.8BR beamline. The spectrum obtained with 8 SDDs is shown in Fig. 7. The absolute energy calibration was performed with K_α fluorescence X-rays from titanium (4.5 keV) and nickel (7.5 keV) foils induced by the beam particles. Furthermore we installed an iron foil at the target position to have fluorescence X-rays at an energy around 6.5 keV. As shown in the lower panel of Fig. 7, we obtained the energy resolution (FWHM) for different three energies. The dotted line in the figure is an empirical formula, $2.35\omega\sqrt{W_N^2 + FE/\omega}$, where E , ω , W_N , and F are incident X-ray energy, electron-hole pair creation energy, noise constant and Fano factor, respectively. The energy dependence is well understood by the known formula. We achieved an energy resolution of 150 eV in FWHM at an energy for kaonic L_α lines in ^3He and ^4He , which is better than that of KEK-PS E570 of 185 eV. Signal to noise ratio for the calibration spectrum in the commissioning is also higher than that of E570 by a factor of 3. As a result of the beam commissioning, good performance of the SDDs was achieved in realistic conditions.

§6. Cylindrical detector system

A schematic view of the Cylindrical Detector System (CDS) with the target system is shown in Fig. 8. The CDS mainly consists of the solenoid magnet, the Cylindrical Drift Chamber (CDC), and the Cylindrical Detector Hodoscope (CDH). The decay particles from the target are reconstructed by the CDC which operates in a magnetic field of 0.7 T provided by the solenoid magnet. The CDH is used for particle identification and as a charged particle trigger. A Time Projection Chamber (TPC) with Thick Gas Electron Multipliers (TGEMs), a Backward Proton Chamber (BPC), and a Backward Proton Detector (BPD) are new detectors for the in-flight experiments. In order to realize an efficient measurement of the decay mode $K^- pp \rightarrow p\pi\Sigma$, the TPC has been developed as an inner tracker for the E15 upgrade which is installed between the target and the CDC. The BPC and the BPD have been developed aiming to reconstruct backward going particles which cannot be detected by the CDC. The BPC and the BPD, which are installed just upstream of the target system, enable measurement of a proton emitted from the $\Lambda(1405) \rightarrow \pi^0 \Sigma^0$ decay mode ($\Sigma^0 \rightarrow \gamma \Lambda \rightarrow \gamma \pi^- p$) by the time-of-flight method.

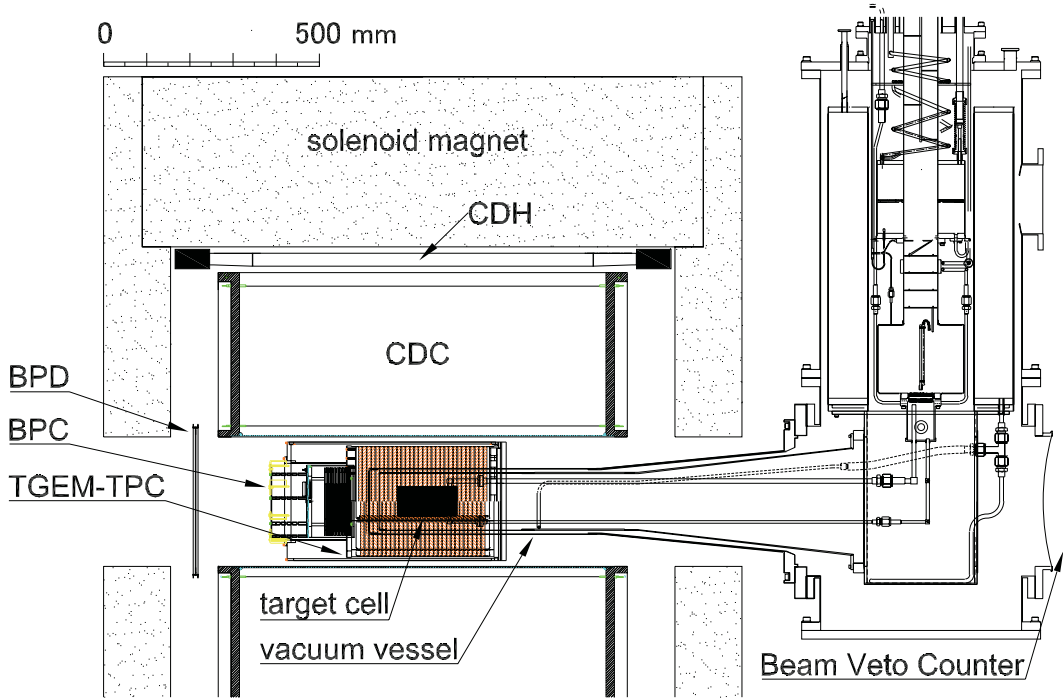


Fig. 8. Schematic view of the CDS with the target system.

6.1. Solenoid magnet

The spectrometer magnet of the CDS is of a solenoidal type, whose bore diameter is 1.18 m and the length is 1.17 m with an overall weight of 23 tons. Design of the solenoid magnet is shown in Fig. 9. The solenoid magnet is located on the final focus

point of the K1.8BR beam line. The magnet provides the uniform field strength inside the tracking volume ($|z| < 420$ mm), whose strength is 0.7 T at the center of the magnet.

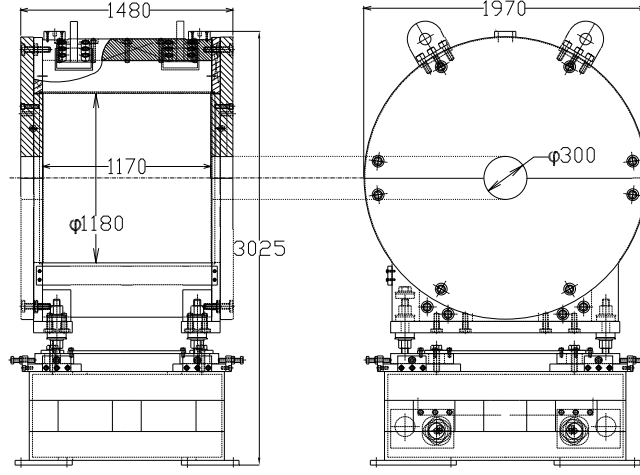


Fig. 9. Design of the solenoid magnet.

6.2. Cylindrical drift chamber

The CDC is located inside the solenoid magnet. The CDC reconstructs charged particle tracks from the target region and provides their momenta with the magnetic field of the solenoid magnet. The outer radius of the CDC is 530 mm, the inner radius 150 mm, and the total length 950 mm. The effective wire length of axial layers is 838.8 mm. The angular coverage of the CDC is $49^\circ < \theta < 131^\circ$ corresponding to a solid angle coverage of 66% of 4π .

The CDC consists of two aluminum end-plates of 20 mm thickness, a 1 mm thick CFRP cylinder as the inner wall of the CDC, and six aluminum posts which are placed outside the tracking volume, as shown in Fig. 10. The CDC uses gold-plated tungsten of $30 \mu\text{m}\phi$ for the sense wires, and gold-plated aluminum of $100 \mu\text{m}\phi$ for the field and guard wires. These wires are supported by feedthroughs with a bushing inserted at the end. Bushes with an $80 \mu\text{m}\phi$ hole are used for the sense wires, so the precision of the wire positioning is $\sim 25 \mu\text{m}$. For the potential and guard wires, bushes with a $200 \mu\text{m}\phi$ hole are used. The CDC has 15 layers of small hexagonal cells with a typical drift length of 9 mm, which are grouped into 7 super layers as shown in Fig. 11. Table III gives the detailed parameters of the wire configuration. The layers are in the radial region from 190.5 mm (layer #1) to 484.5 mm (layer #15). The 8 stereo layers tilted by about 3.5° are used to obtain longitudinal position information. The number of readout channels is 1816 and the total number of wires in the CDC is 8064.

The argon(50%)-ethane(50%) mixed gas is used at 1 atm as the drift gas of the CDC. A high voltage is applied to the field and guard wires, and the sense wires are kept at ground potential. For the first super layer (A1) and the second one (U1) a

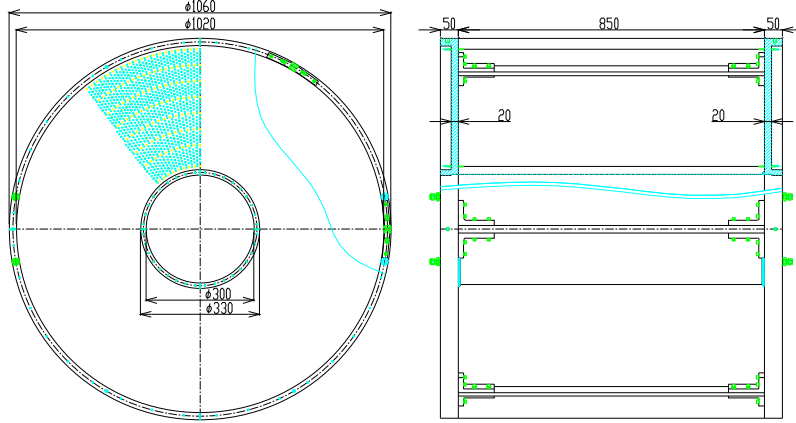


Fig. 10. Design of the CDC. The CDC consists of two aluminum end-plates, a 1 mm thick CFRP cylinder as the inner wall, and six aluminum posts which are placed outside the tracking volume.

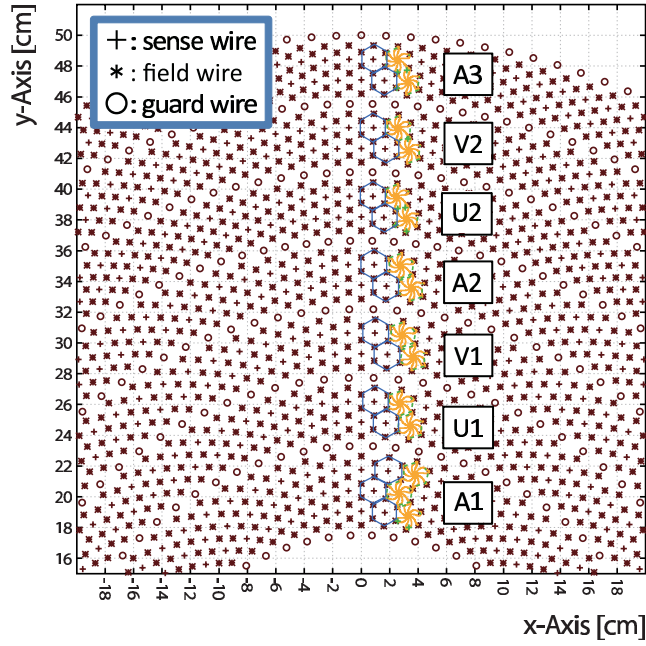


Fig. 11. Cell structure of the CDC.

high voltage of -2.8 kV is applied to the potential wires, and -2.7 kV to the potential wires of the other super layers. Also -1.5 kV, -1.8kV, and -0.6 kV is applied to the inner-most, the outer-most, and the other guard wires, respectively. The read-out electronics of the CDC consists of a preamp card with ASDs (SONY-CXA3653Q, $\tau = 16$ ns), a LVDS-ECL converter, and a TDC, the same as those for the beam line chambers. A typical resolution of 200 μm is obtained.

Table III. Wire configuration of the CDC.

super layer	layer	wire direction	radius (mm)	cell width (degree)	cell width (mm)	stereo angle (degree)	signal channels per layer
A1	1	X	190.5	5.00	16.7	0	72
	2	X'	204.0		17.8	0	
	3	X	217.5		19.0	0	
U1	4	U	248.5	4.00	17.3	-3.55	90
	5	U'	262.0		18.3	-3.74	
V1	6	V	293.0	3.60	18.4	3.77	100
	7	V'	306.5		19.3	3.94	
A2	8	X	337.5	3.00	17.7	0	120
	9	X'	351.0		18.4	0	
U2	10	U	382.0	2.40	16.0	-3.28	150
	11	U'	395.5		16.6	-3.39	
V2	12	V	426.5	2.25	16.7	3.43	160
	13	V'	440.0		17.3	3.54	
A3	14	X	471.0	2.00	16.4	0	180
	15	X'	484.5		16.9	0	

6.3. Cylindrical Detectors Hodoscope

The CDH is a segmented plastic scintillation counter used for the charged particle trigger and particle identification. The CDH is located at a radius of 544 mm from the beam axis covering a polar angle range from 54 to 126 degrees corresponding to a solid angle coverage of 59% of 4π .

The CDH consists of 36 modules, individually mounted on the inner wall of the solenoid magnet. The scintillators are made of Eljen EJ-560, whose dimensions are 790 mm in length, 99 mm in width, and 30 mm in thickness. The scintillation light is transferred through light guides to a pair of photomultipliers attached to the top and bottom ends. For the CDH, Hamamatsu Photonics R7761 fine-mesh photomultipliers with a 1.5 inch diameter and 19 dynode stages are selected. The CDH is operated under the magnetic field of 0.7T, with PMT gain of $\sim 10^6$ typically. The measured time resolution of the CDH without a magnetic field is an average of 71 ± 3 ps (σ), which is obtained with cosmic ray data.

6.4. TGEM time projection chamber

The TPC with TGEMs has been developed to perform precise vertex-reconstruction for hyperon decays such as Λ and Σ^\pm , as an inner tracker of the CDS. The TPC is installed between the target and the CDC. For the TPC, the spatial resolution in the Z direction should be less than 1 mm, and the material budget in the CDC acceptance should be minimized as much as possible.

The design of the TPC is shown in Fig. 12. The TPC is cylindrical in shape with inner diameter 170 mm, outer 280 mm, and filled with P-10 gas (90% Ar+ 10% CH₄) at atmospheric pressure. The drift length is 30 cm in a field cage made from double-sided Flexible Printed Circuits (FPC) having staggered strip electrodes having a width of 8 mm and pitch of 10 mm, which are connected with 1 M Ω resistors. A drift field of 150 V/cm is applied to the field cages. For amplification, a dou-

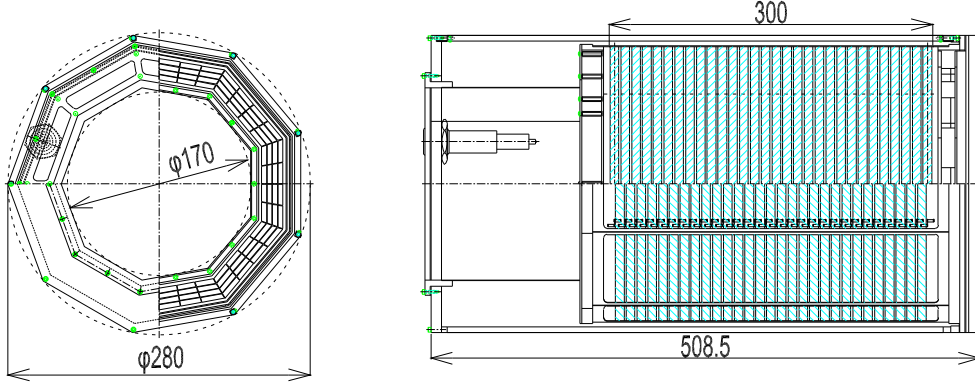


Fig. 12. Design of the TGEM-TPC.

ble or triple-TGEM structure is used; the TGEM is economically constructed from double-clad 400- μm -thick FR4 plate using standard Printed Circuit Board (PCB) techniques, and has mechanically drilled holes.¹⁸⁾ In order to reduce both the energy and the propagation probability of the discharge, the TGEM for the TPC has a nonagonal shape whose sides are subdivided into three sectors and separately connected externally to the voltage supply through high-value resistors. High voltages are applied to the double/triple-TGEM resistor chain through connectors penetrating the end cap. The gain of these nonagonal TGEMs is greater than 10^4 with graphite electrodes having a resistance of about $30 \Omega/\square$ both with double- and triple-TGEM configurations as shown in Fig 13. The graphite-electrode TGEM is a new development to protect the detector and the readout electronics from damage by any occasional discharge. The layout of the readout system is also nonagonal and is divided into 4×4 pads on each side with 4 mm-long and 20 mm-wide pads printed on a standard PCB (the total number of readout channels is 144). For the TPC front-end electronics, preamplifier cards with ASDs (SONY-CXA3653Q, $\tau = 80 \text{ ns}$) are used, i.e., the TPC provides only beam-direction information of tracks. The TPC will be completed in 2012.

6.5. Detectors for backward protons

The BPC and BPD are installed just upstream of the target system aiming to reconstruct backward going particles, such as pions and protons, which cannot be detected by the CDC.

The BPC is a compact and circular planar drift chamber located just before the target system, whose size is 168 mm in diameter and 89.7 mm in height. Figure 14 shows a design of the BPC. The BPC consists of 8 layers with a $XX'YY'XX'YY'$

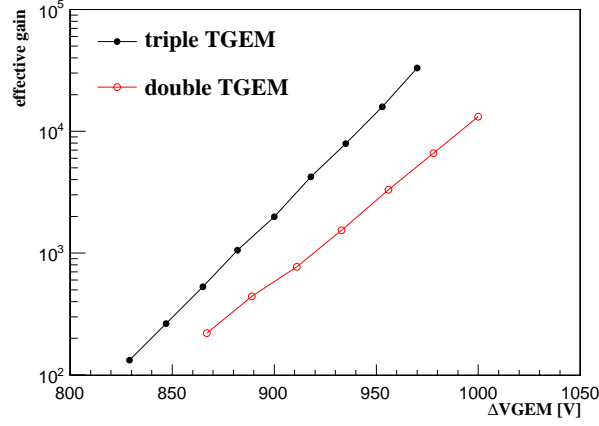


Fig. 13. Effective gains of the nonagonal TGEMs with the graphite electrode as a function of the voltage across each TGEM. The data for the double- and triple-TGEM configurations are shown.

configuration, where wires of the Y layer are tilted by 90 degrees. Each layer contains 15 sense wires with a drift length of 3.6 mm corresponding to an effective area of $111.6 \text{ mm}\phi$. The number of readout channels is 120. The cathode planes are made of $9 \mu\text{m}$ carbon aramid foil, and sense and potential wires of the BPC are the same as those for the beam line chambers. Also the read-out electronics and gas mixture are the same as those for the beam line chambers. The operational voltage of the BPC is set to be -1.45 kV onto the potential wires and the cathode planes. Typical position resolution of the BPC is $150 \mu\text{m}$.

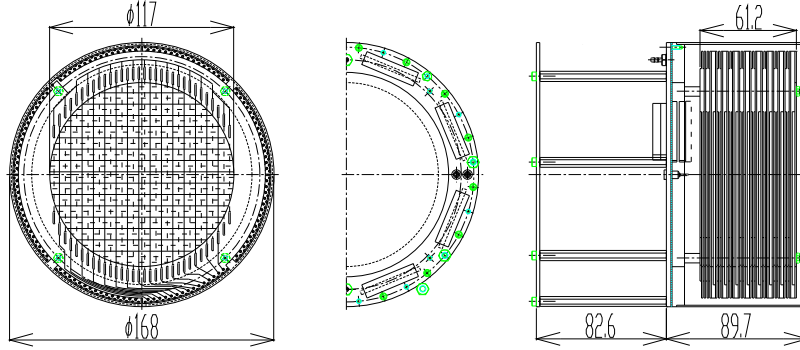


Fig. 14. Design of the BPC.

The BPD is a plastic scintillator hodoscope array and is placed 0.5 m upstream from the final focus point, inside the solenoid magnet. The size of the BPD is 350 mm (horizontal) \times 340 mm (vertical) segmented into 70 units. Each scintillation counter, made of Eljen EJ230, is $5 \text{ mm} \times 5 \text{ mm} \times 340 \text{ mm}$. Due to the strong magnetic field and a limited space, Multi-Pixel Photon Counters (MPPC) with a $3 \text{ mm} \times 3 \text{ mm}$ sensitive area are employed (Hamamatsu S10362-33-050C). The MPPCs are put on

both sides of each slab. Signals from the MPPCs are read out by fast timing amps (Ortec FTA820). Using a prototype detector, a time resolution of 150 ps has been achieved, which is sufficient to identify a particle in the backward direction. The BPD will be completed in 2012.

§7. Neutron time-of-flight counter and beam sweeping magnet

The neutron TOF counter, placed ~ 15 m away from center of the target at 0 degrees with respect to the beam direction, detects a forward neutron generated by the (in-flight K^- , n) reaction. The neutron TOF counter is an array of scintillator counters used by KEK-PS E549, which was reassembled for the E15 experiment. The kaon beam is swept out from the acceptance of the neutron counter by a sweeping magnet placed just after the CDS in order to guarantee sufficient neutron detection efficiency. Charged particles into the acceptance of the neutron counter, such as those generated on the wall of the beam sweeping magnet, are vetoed by a TOF stop counter located just upstream of the neutron counter. In addition, a beam veto counter is installed between the CDS and the beam sweeping magnet to reduce fake triggers caused by the decay of beam kaons after the target.

In order to measure the ${}^3\text{He}(K^-, p)$ reaction as well as the (K^-, n) one, a proton TOF counter is installed. The comparison of the two kinds of missing-mass spectra will provide us unique information on the isospin dependence of the kaon-nucleus (\bar{K} -NN) interaction. The proton counter is located alongside the TOF stop counter, as an extended wall of the TOF stop counter, on the opposite side of a beam dump to which the beam is bent by the beam sweeping magnet. Figure 15 shows a schematic view of the neutron counter, the TOF stop counter, and the proton counter.

7.1. Neutron time-of-flight counter

A forward neutron generated by the (in-flight K^- , n) reaction is detected by the neutron TOF counter located 14.7 m away from the final focus point in which the experimental target is installed. The neutron TOF counter consists of an array of scintillator counters, which has an effective volume of 3.2 m (horizontal) \times 1.5 m (vertical) \times 0.35 m (depth) segmented into 16-columns (horizontal) \times 7-layers (depth) units. The acceptance of the neutron counter is $\pm 6.2^\circ$ in the horizontal direction and $\pm 2.9^\circ$ in the vertical. Each scintillation counter has dimensions of 20 cm (width) \times 150 cm (height) \times 5 cm (thickness) with Hamamatsu H6410 photomultipliers with a 2 inch diameter, which are attached to both the long sides of scintillator through a Lucite light guide. The scintillators for the first three layers are made of Saint-Gobain BC408, and the other four layers are made of Saint-Gobain BC412. The time resolution of the neutron counter, measured with cosmic rays, is an average of 92 ± 10 ps (σ). The detection efficiency for a ~ 1 GeV/ c neutron is expected to be $\sim 35\%$ from the Monte Carlo simulation by the GEANT4 tool kit.¹⁹⁾

7.2. Beam sweeping magnet

A dipole magnet named Ushiwaka which was used in the $\pi 2$ beam line of the 12 GeV proton synchrotron at KEK is used as the beam sweeping magnet. It is located

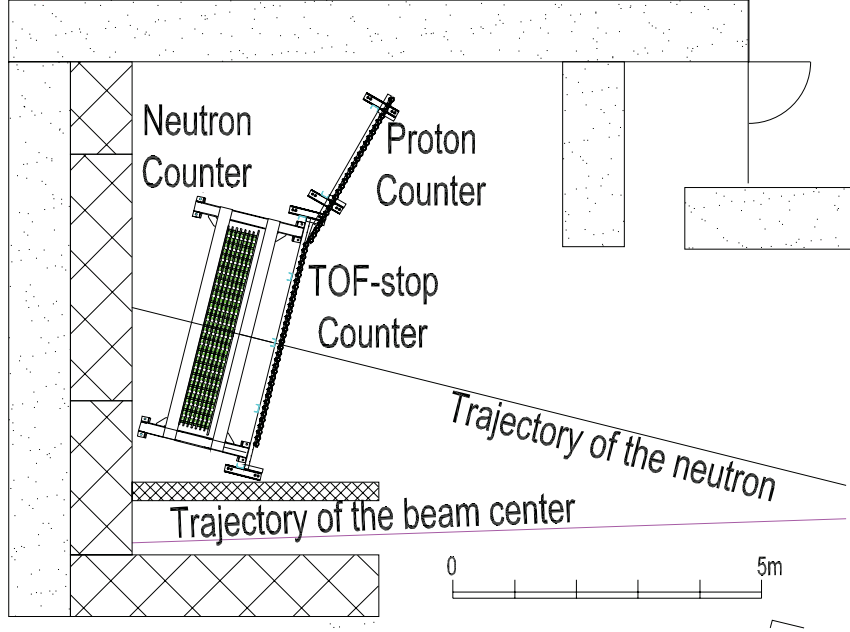


Fig. 15. Schematic view of the neutron counter, the TOF stop counter, and the proton counter. The neutron counter is located 14.7 m away from the final focus position.

just downstream of the CDS. The magnet has an aperture of 82 cm (horizontal) \times 40 cm (vertical) and a pole length of 70 cm, and is capable of providing a maximum field of 1.6 T. In order to sweep the beam away from the neutron counter acceptance window and transfer the beam to the beam dump, the magnet provides a field strength of ~ 1.2 T at the center of the magnet.

7.3. TOF stop counter

The TOF stop counter is located upstream of the neutron counter, 14.0 m away from the final focus point. This counter is used as a charge veto counter for the neutron detector. It has an effective area of 3.4 m (horizontal) \times 1.5 m (vertical) segmented into 34 units. Each scintillation counter has dimensions of 10 cm (width) \times 150 cm (height) \times 3 cm (thickness), and is equipped with two Hamamatsu H6410 photomultipliers with a 2 inch diameter attached to both long sides of the scintillator through a Lucite light guide. The scintillators are of Saint-Gobain BC408 type. The measured time resolution is an average of 84 ± 9 ps (σ) with cosmic ray data.

7.4. Proton time-of-flight counter

The proton TOF counter is installed as the extended wall of the TOF stop counter. It has an effective area of 2.7 m (horizontal) \times 1.5 m (vertical) segmented into 27 units. The momentum acceptance for the proton is over 1.0 GeV/c. Each scintillation counter is the same as that for the TOF stop counter. The time resolution of the proton counter, obtained from cosmic ray data, is an average of 75 ± 6 ps (σ).

7.5. Beam veto counter

The beam veto counter is installed between the CDS and the beam sweeping magnet. The size of the beam veto counter is 315 mm (height) \times 315 mm (width) \times 10 mm (thickness) made of Saint-Gobain BC408. The scintillation light transferred through a light guide is read by a Hamamatsu H6154 photomultiplier, whose photocathode diameter is 2 inches and the dynode structure is a fine-mesh type. A high voltage bleeder of the photomultiplier is modified to supply enough current to the last three dynodes.

§8. Trigger and data acquisition

8.1. Trigger

From experimental requirements, the dedicated hardware trigger is applied to each experiment. The kaon beam trigger is common for all experiments, whereas, main triggers for the in-flight experiment (E15 and E31) and for the stopped- K^- experiment with the SDDs (E17) are substantially different. The E15 and E31 experiments use the 1.0 GeV/ c kaon beam, and detect a forward neutron generated by the ^3He or $d(K^-, n)$ reaction. The E17 experiment uses the kaon beam of 0.9 GeV/ c which is stopped in the liquid target by using degraders located just upstream of the target system.

kaon beam trigger

The elementary beam trigger is constructed by coincidence signals from the beam line counters, the BHD and T0. The kaon beam trigger (K_{beam}) is selected from the beam trigger by using the kaon identification counter, i.e., a veto signal of the AC (\overline{AC}) defines the kaon beam. It is to be noted that (anti-) protons in the beam are eliminated upstream of the beam line by using the ESS1, CM1, and CM2. A logical expression of the kaon beam trigger is given as,

$$(K_{beam}) \equiv (BHD) \otimes (T0) \otimes (\overline{AC}).$$

E15 main trigger

A two-level trigger logic for the $^3\text{He}(\text{in-flight } K^-, n)$ reaction is applied. In order to reconstruct the expected decay $K^- pp \rightarrow \Lambda p \rightarrow p\pi^- p$ using the CDS, the event with two or more CDH hits (CDH_2) is selected from the kaon beam trigger in the first level ($E15_{1st}$). In addition, no hit on the beam veto counter (\overline{BVC}) is required to reduce the trigger rate. In the second level ($E15_{2nd}$), the event with the forward neutron is chosen by requiring a neutron counter hit (NC) and a veto signal of the TOF stop counter (\overline{TOF}). The E15 main trigger is given as,

$$\begin{aligned} (E15_{1st}) &\equiv (K_{beam}) \otimes (CDH_2) \otimes (\overline{BVC}), \\ (E15_{2nd}) &\equiv (E15_{1st}) \otimes (NC) \otimes (\overline{TOF}). \end{aligned}$$

E17 main trigger

A two-level trigger logic is applied in order to measure X-rays from the kaonic helium 3 and 4 atoms. The stopped- K^- trigger ($K_{stopped}$) is generated by the

signal from E0 and the veto-signal from the beam veto counter with the kaon beam definition:

$$(K_{stopped}) \equiv (K_{beam}) \otimes (E0) \otimes (\overline{BVC}).$$

For the first-level trigger ($E17_{1st}$), one or more CDH hits (CDH_1) is required in order to reduce the trigger rate and obtain the reaction vertex. A hit in the SDD is required in the second level, because the timing of the SDD signal from the shaping amplifier is too late for the trigger timing of the first level. Therefore the E17 main trigger is,

$$\begin{aligned} (E17_{1st}) &\equiv (K_{stopped}) \otimes (CDH_1), \\ (E17_{2nd}) &\equiv (E17_{1st}) \otimes (SDD). \end{aligned}$$

E31 main trigger

A two-level trigger logic for the d(in-flight K^- , n) reaction is applied. Since the E31 measures $\Lambda(1405)$ decays into $\pi^0 \Sigma^0 \rightarrow \pi^0 \gamma \Lambda \rightarrow \pi^0 \gamma \pi^- p$ and $\pi^\pm \Sigma^\mp \rightarrow \pi^\pm \pi^\mp n$ using the CDS in addition to the forward neutron, the trigger logic is the same as for the E15 trigger except for requiring one or more CDH hits in the first level. Thus the E31 main trigger is,

$$\begin{aligned} (E31_{1st}) &\equiv (K_{beam}) \otimes (CDH_1) \otimes (\overline{BVC}), \\ (E31_{2nd}) &\equiv (E31_{1st}) \otimes (NC) \otimes (\overline{TOF}). \end{aligned}$$

8.2. Data acquisition system

The on-line data acquisition system (DAQ) for the experiments at K1.8BR consists of the TKO, VME, and PC Linux. The signals from the detectors are fed into ADC and TDC modules slotted into the TKO crates. In the K1.8BR experiments, 10 TKO crates are used and they are parallel read from VME-SMP (Super Memory Partner) via TKO SCH (Super Controller Head). The data stored in a buffer memory of the SMP is transferred to the DAQ-PC through the SBS Bit3 VME-to-PCI bridges. Additionally the E17 experiment uses an another system which consists of the VME (flash-ADC modules) and PC Linux for the read-out of the SDDs. The data is written to the disk on the DAQ-PC, and transferred to a PC cluster server at RIKEN via Internet.

§9. Spectrometer performance

The quality of the secondary kaon beam is key for all of the experiments at K1.8BR. We have optimized the beam line from 2009 to obtain an intense and good K/π -separated kaon beam by tuning the beam line spectrometer. During a commissioning run in February 2012, beam line commissioning for 1.0 GeV/ c was accomplished and optimized parameters of the spectrometer were obtained. Details of the beam line performance are described in Ref.²⁰⁾ It should be noted that the 1.0 GeV/ c kaon yield normalized by the accelerator power of 1.0 kW was obtained to be 10 k / spill with the K/π ratio of 0.3, typically.

Commissioning of the CDS with a liquid ^4He target was also conducted in February 2012. Charged particles from the target were tracked by the CDC, and momentum information was obtained with the magnetic field of 0.7 T provided by the solenoid magnet. The momentum resolution of the CDC is shown in Fig. 16 which is estimated by a Monte Carlo simulation using the GEANT4 toolkit. In the simulation, the obtained resolution of the CDC together with energy losses and scatterings in the detector materials are taken into account. The CDC p_t -resolution is evaluated to be $8.4\% p_t \oplus 1.1\% / \beta$. Using the simulation, the vertex resolution of the CDC is also estimated to be 2.1 mm and 5.0 mm for perpendicular and parallel direction to the beam axis. The event vertex is obtained from trajectories of the beam and the secondary-particles which are reconstructed by the BPC and the CDC, respectively. The reconstructed beam-profile at the final focus point is shown in Fig. 17, and Fig. 18 demonstrates the event-vertex reconstruction in which the liquid helium target cell and transfer pipes are clearly seen.

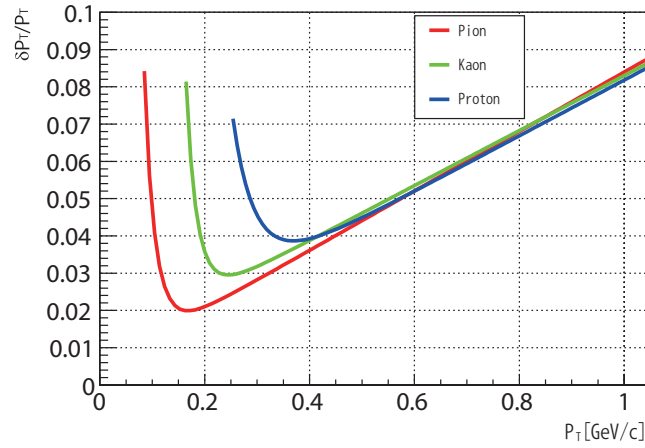


Fig. 16. Momentum resolution of the CDC estimated by the Monte Carlo simulation by taking into account the obtained resolution of the CDC together with detector effects. The resolution for pion, kaon and proton are shown.

The identification of the secondary charged particle was performed by the CDH using TOF measurements together with T0. Here the flight length was calculated from the event vertex and the particle trajectory. Figure 19 shows the distributions of the momentum versus $1/\beta$ corresponding to the obtained TOF resolution of 160 ps (σ). Pions, protons, and deuterons are clearly separated. Using the momentum reconstruction and the particle identification, invariant mass of $p\pi^-$ was reconstructed as shown in Fig. 20. A clear peak of $\Lambda \rightarrow p\pi^-$ decay can be seen. As direct demonstration of the spectrometer performance, the mass resolution of $\Lambda \rightarrow p\pi^-$ decay was compared to the expectations from the detailed detector simulation. The centroid of Λ is obtained as $1113.3 \pm 0.1 \text{ MeV}/c^2$ (known to be $1115.7 \text{ MeV}/c^2$) with a Gaussian resolution of $3.3 \pm 0.1 \text{ MeV}/c^2$, whereas the expected centroid is $1114.2 \text{ MeV}/c^2$ with the resolution of $3.2 \text{ MeV}/c^2$; the CDS performance has been reproduced by the simulation and satisfied the experimental requirements for the E15 experiment.

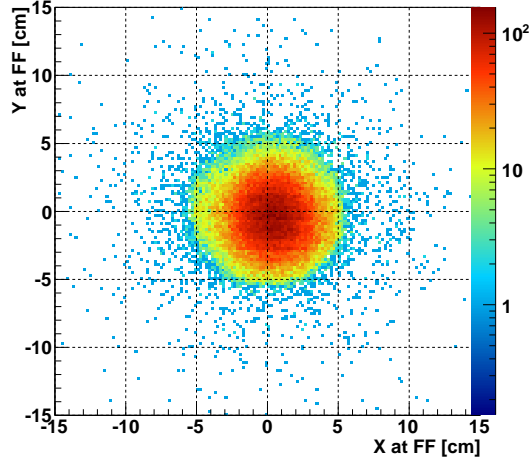


Fig. 17. Beam profile of the kaons at the final focus point reconstructed by the BPC.

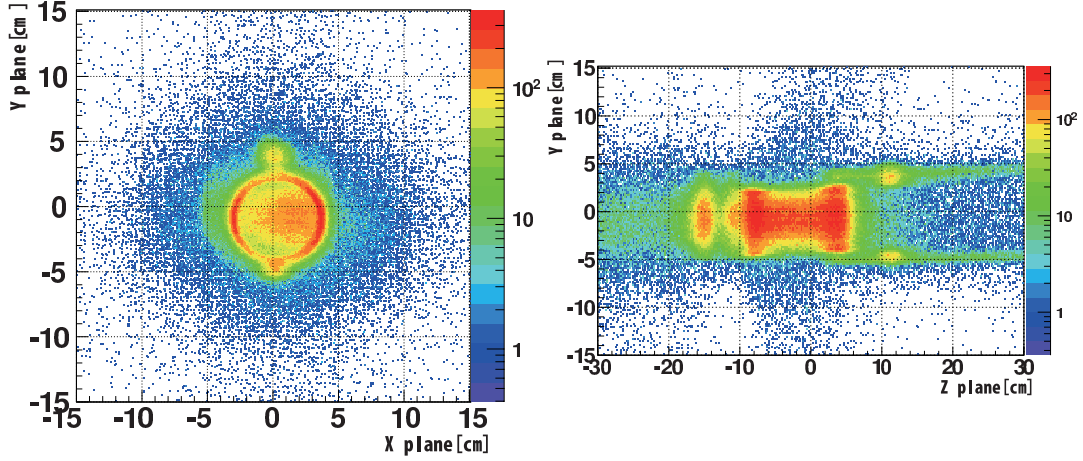


Fig. 18. Event vertex with the pion beam reconstructed by the CDS. The cross section of perpendicular (left) and parallel (right) direction to the beam axis are shown. The liquid helium target cell and transfer pipes are clearly seen.

§10. Summary

A new spectrometer system was designed and constructed at the secondary beam-line K1.8BR in the hadron hall of J-PARC. The experiments at the K1.8BR beam line aim to investigate $\bar{K}N$ interactions and \bar{K} -nuclear bound systems. The E15 [kaonic-nuclei search via ${}^3\text{He}(\text{in-flight } K^-, n)$], the E17 [kaonic-atom X-ray measurement with stopped- K^-], and the E31 [spectroscopic study of $\Lambda(1405)$ via $d(K^-, n)$] experiments were proposed and approved for the K1.8BR beam line. The spectrometer consists of the high precision beam line spectrometer, the liquid target system, the Cylindrical Detector System that surrounds the target to detect the decay particles from the target region, and the neutron time-of-flight counter located

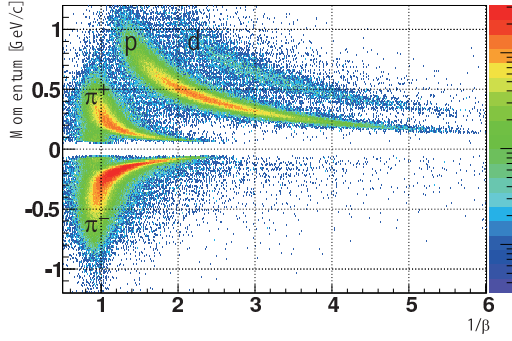


Fig. 19. Distributions of the momentum versus $1/\beta$ obtained by using the CDS.

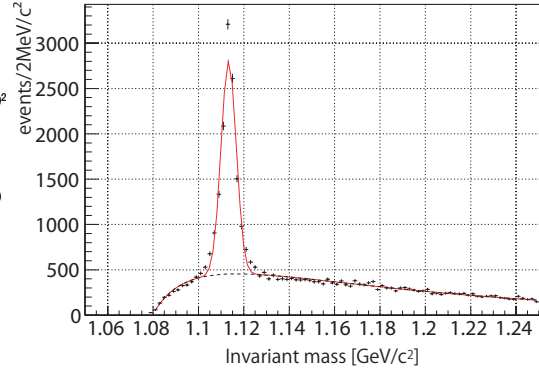


Fig. 20. Invariant mass spectrum of $p\pi^-$. The spectrum is fitted with a Gaussian and a background curve. The displaced vertex cut of 2 cm is applied.

~ 15 m away from the target position. Commissioning of the beam line spectrometer and the CDS were successfully performed with a 1.0 GeV/ c kaon beam in February 2012, and expected performance has been confirmed. Construction of the neutron time-of-flight counter array, the last piece of the K1.8BR spectrometer system, was completed in May 2012. Thus the experiments at K1.8BR are ready now, and physics output will be reported in near future.

Acknowledgments

We gratefully acknowledge all the staff members of J-PARC. Especially, we would like to sincerely thank them for a great deal of effort to recover from catastrophic damages caused by the earthquake on March 11, 2011. This work was supported by RIKEN, KEK, RCNP, the Grant-in-Aid for Scientific Research on Priority Areas [No. 17070005 and No. 20840047], the Grant-in-Aid for Specially Promoted Research [No. 20002003], the Grant-in-Aid for Young Scientists (Start-up) [No. 20028011], the Grant-in-Aid for Scientific Research on Innovative Areas [No. 21105003], and the Austrian Science Fund (FWF) [P20651-N20].

References

- 1) M. Iwasaki, *et al.*, Phys. Rev. Lett. **78** (1997), 3067;
G. Beer, *et al.*, Phys. Rev. Lett. **94** (2005), 212302;
M. Bazzi, *et al.*, Phys. Rev. B **704** (2011), 113.
- 2) A. D. Martin, Nucl. Phys. B **179** (1981), 33.
- 3) Y. Akaishi and T. Yamazaki, Phys. Rev. C **65** (2002), 044005;
Y. Akaishi and T. Yamazaki, Phys. Lett. B **535** (2002), 70;
T. Yamazaki, Y. Akaishi, Phys. Rev. C **76** (2007), 045201.
- 4) N.V. Shevchenko, A. Gal, J. Mares, and J. Revai, Phys. Rev. C **76** (2007), 044004;
Y. Ikeda and T. Sato, Phys. Rev. C **79** (2009), 035201.
- 5) D. Jido *et al.*, Nucl. Phys. A **725** (2003), 181;
V. K. Magas, E. Oset, A. Ramos, and H. Toki, Phys. Rev. C **74** (2006), 025206;
A. Dote, T. Hyodo, and W. Weise, Phys. Rev. C **79** (2008), 014003.
- 6) O. Braun *et al.*, Nucl. Phys. B **129** (1977), 1;

- M. Niiyama *et al.*, Phys. Rev. C **78** (2008), 035202.
- 7) M. Agnello *et al.*, Phys. Rev. Lett. **94** (2005), 212303;
T. Kishimoto *et al.*, Prog. Theor. Phys. **118** (2007), 181;
T. Yamazaki *et al.*, Phys. Rev. Lett. **104** (2010), 132502.
- 8) J-PARC E15 proposal : http://j-parc.jp/NuclPart/pac_0606/pdf/p15-Iwasaki.pdf
- 9) J-PARC E17 proposal : http://j-parc.jp/NuclPart/pac_0606/pdf/p17-Hayano.pdf
- 10) S. Okada *et al.*, Phys. Lett. B **653** (2007), 387.
- 11) J-PARC E31 proposal : http://j-parc.jp/NuclPart/pac_0907/pdf/Noumi.pdf
- 12) J. R. Sanford and C. L. Wang, *BNL-AGS internal reports* 11279 and 11479 (1976);
A. Yamamoto, *KEK Report* NO.81-13 (1981).
- 13) O. Sasaki and M. Yoshida, *IEEETrans. Nucl. Sci.*, **46** (1999) 1871.
- 14) M. Iio *et al.*, arXiv:ins-det/1205.2183 (accepted to *Nucl. Instrum. Meth. A*).
- 15) M. Sato *et al.*, *Nucl. Instrum. Meth.* **A606** (2009) 233.
- 16) E. Gatti and P. Rehak, *Nucl. Instrum. Meth.* **A225** (1984) 608.
- 17) M. Bazzi *et al.*, Phys. Lett. B **681** (2009), 310.
- 18) R. Chechik *et al.*, *Nucl. Instrum. Meth.* **A535** (2004) 303;
C. Shalem *et al.*, *Nucl. Instrum. Meth.* **A558** (2006) 475.
- 19) S. Agostinelli, *et al.*, *Nucl. Instrum. Meth.* **A506** (2003) 250.
- 20) M. Ieiri *et al.*, PTEP **xxx** (2012) xxx.